THE ASTROPHYSICAL JOURNAL, 301:320–330, 1986 February 1

APERTURE SYNTHESIS OBSERVATIONS OF THE 21 CENTIMETER ZEEMAN EFFECT TOWARD CASSIOPEIA A

U. J. SCHWARZ
Kapteyn Astronomical Institute

T. H. TROLAND
Physics and Astronomy Department, University of Kentucky

J. S. ALBINSON AND J. D. BREGMAN
Netherlands Foundation for Radio Astronomy

W. M. GOSS
Kapteyn Astronomical Institute

AND

CARL HEILES
Astronomy Department, University of California, Berkeley
Received 1985 January 11; accepted 1985 July 16

ABSTRACT

We have used the Westerbork synthesis radio telescope to perform an improved sensitivity study of the 21 cm H I Zeeman effect toward Cas A. We present synthesis maps of the line-of-sight magnetic field strength for velocities corresponding to the Perseus arm absorption features. Considerable spatial structure exists in these maps, with measured field strengths exceeding 40 μG at some positions in front of the source. No significant reversals in field direction are apparent. Peaks in magnetic field strength often coincide in position with clumps of molecular gas that appear in H_2CO and in OH synthesis maps of Cas A. The magnetic field peaks arise in clumps of higher density H I gas that are associated with the molecular clumps. Thus, we have detected for the first time an increase in magnetic field strength with interstellar gas density. Magnetic effects are likely to have an important influence upon the dynamics of the H I clumps and to a lesser extent upon the molecular clumps. High magnetic fields in the direction of Cas A may arise because the line of sight passes through, or close to, regions of star formation.

Subject headings: interstellar: magnetic fields — nebulae: individual — nebulae: supernova remnants — radio sources: 21 cm radiation — Zeeman effect

I. INTRODUCTION

The cone of interstellar space having the Sun at its apex and Cas A at its base is one of the best-studied regions of the Galaxy. Extending out ~ 3 kpc in the direction $(l, b) = (111\overset{\circ}{.}7, -2\overset{\circ}{.}1)$ and having an apex angle of $\sim 5'$, this region includes absorbing atomic and molecular gas at velocities associated with the Local and Perseus spiral arms. CO emission at these same velocities also arises in the cone and in adjacent directions as well (Troland, Crutcher, and Heiles 1985).

Unlike most regions of the interstellar medium, the magnetic field strength is known in the interstellar clouds that occupy this cone of space. From single-dish observations of the Zeeman effect, Verschuur (1969*a*) inferred line-of-sight magnetic field strengths of $+20$ and $+10$ μG for the major Perseus arm H I absorption features centered ~ -37 and -47 km s^{-1}, respectively. (Henceforth, we refer to these as the low-velocity and the high velocity features, respectively.) Heiles and Stevens (1985) have recently detected the Zeeman effect in the four principal Perseus arm OH absorption lines centered ~ -48, -46, -40, and -37 km s^{-1}. These single-dish measurements yield field strengths of about $+9$ μG for each of the four components. The absence of a Zeeman effect in the Local arm H I absorption feature led Troland and Heiles (1982*a*) to set a limit of 0.8 μG for this region.

The presence of a readily detectable H I Zeeman effect in the Cas A Perseus arm absorption features provides an unusual opportunity to apply aperture synthesis techniques to the study of the interstellar magnetic field. We have previously reported upon the first such study (Bregman *et al.* 1983; hereafter Paper I). Using the Westerbork synthesis radio telescope (WRST), we obtained maps of the Perseus arm H I absorption across the face of the source in both Stokes parameters I and V. From these maps, we derived the magnitude of the Zeeman effect and, hence, of the line-of-sight magnetic field strength at different positions in front of Cas A. Here, we report upon the second aperture synthesis study of the magnetic field in the direction of Cas A. Using the same telescope system, we have now achieved a factor of 2 increase in sensitivity, and we have applied new data analysis procedures to create the first detailed maps of the magnetic field strength in the direction of this source.

The Cas A observations reported in Paper I are of limited sensitivity. Nonetheless, they establish that the magnetic fields in the low- and high velocity features are relatively uniform over angular scales of $1\overset{'}{.}5$ to $5'$ (1.3–4.4 pc at a distance of 3 kpc). That is, no reversal of the field occurs across the face of the source at either velocity, and variations in the line-of-sight field strength across the source are less than a factor of 2 for the angular scales sampled. Some indications do exist in these data for a field-strength gradient in the low-velocity feature; however, the sensitivity is too low to establish this effect with certainty.

Since the time of our original aperture synthesis study (Paper I), a considerable body of data has accumulated concerning the small-scale structure of atomic and molecular species in the direction of Cas A. Kalberla, Schwarz, and Goss (1985) have used the WSRT to improve upon the H I synthesis maps of Greisen (1973). Goss, Kalberla, and Dickel (1985; hereafter GKD) have also used the WRST to obtain synthesis maps of H_2CO across the face of Cas A; and Bieging and Crutcher (1985) have done the same for OH with the Very Large Array (VLA). Furthermore, Batrla, Walmsley, and Wilson (1984) have mapped NH_3 absorption across Cas A, and Troland, Crutcher, and Heiles 1985) have mapped the CO emission in front and adjacent to the source. Given this wealth of new information, spatially resolved maps of the magnetic field towards Cas A are of particular value because they permit a comparison to be made between the distribution of magnetic field strengths and the structure of the atomic and molecular gas.

II. THE INSTRUMENT AND OBSERVATIONS

Apart from the ability to achieve high angular resolution, an aperture synthesis instrument offers some important advantages over a single dish in detecting the Zeeman effect. These are outlined in § II of Paper I. For this series of observations, we operated the WSRT and the 5120 channel digital-line back end (DLB; Bos, Raimond, and van Someren Greve 1981) as a 20 interferometer system. Each of the 10 "fixed" telescopes (separation 144 m) was correlated with the two "movable" telescopes at the east end of the array. Four 12 hr periods of observations were made, the first two with the distance between fixed and movable telescopes set at 36 m and the second two with this distance set at 72 m. In this way, we synthesized all spacings from 36 to 1440 m in steps of 36 m. The twofold increase in sensitivity relative to the observations of Paper I comes from a doubling of both the integration time and of the number of interferometer pairs.

Each telescope has two orthogonal dipole feeds, x and y. In our observations, the x dipoles were aligned parallel to the celestial equator (P.A. = 90°). When operated in this mode, each pair of telescopes forms four separate polarization interferometers with complex responses as follows:

$$\begin{aligned} R_{xx} &= G_{xx}(I - Qn_{xx}U - e_{xx}jV)\,, \\ R_{xy} &= G_{xy}(e_{xy}I + n_{xy}Q - U + jV)\,, \\ R_{yx} &= G_{yx}(-e_{yx}I + n_{yx}Q - U - jV)\,, \\ R_{yy} &= G_{yy}(I + Q - n_{yy}U - e_{yy}jV)\,. \end{aligned} \tag{1}$$

In these equations, I, Q, U, and V are the complex visibility functions of the Stokes parameters in units of flux density, G represents the complex gain factors of the interferometers, and n and e are complex dipole cross-talk factors of order 0.01 (Weiler and Raimond 1976). The G factors were determined using standard calibration procedures.

We applied van Vleck corrections to the correlation coefficients to allow for the large apparent effect of Cas A on the system noise temperature. We measured the system noise temperature by means of calibrated noise injected into the receiver front ends.

The observations were made with the DLB set to provide 31 frequency channels (without taper) having a velocity resolution of 1.2 km s^{-1}, a velocity separation of 1.0 km s^{-1}, and a total velocity coverage of -58 to -27 km s^{-1} (LSR).

III. DATA ANALYSIS

a) Correction for Instrumental Polarization

After calibration [and ignoring terms of the order $(n, e) \times (Q, U, V)$], the responses of the interferometers become

$$\begin{aligned} R'_{xx}(u, v, f) &= I(u, v, f) - Q(u, v, f)\,, \\ R'_{xy}(u, v, f) &= e_{xy}(u, v)I(u, v, f) - n_{xy}U(u, v, f) + jV(u, v, f)\,, \\ R'_{yx}(u, v, f) &= -e_{yx}(u, v)I(u, v, f) - n_{yx}U(u, v, f) - jV(u, v, f)\,, \\ R'_{yy}(u, v, f) &= I(u, v, f) + Q(u, v, f)\,. \end{aligned} \tag{2}$$

Taking the difference of the R'_{xy} and R'_{yx} correlations, we obtain

$$jV'(u, v, f) = jV(u, v, f) + e(u, v)I(u, v, f)\,, \tag{3}$$

where V' is a distorted V visibility function. In order to recover V, we took channels of V' outside the absorption feature (where V is zero), we averaged these channels, and then we divided them by I averaged over the same channels to obtain $e(u, v)$. Next, for each channel we multiplied $I(u, v, f)$ by $e(u, v)$ and subtracted this correlation term from $jV'(u, v, f)$. The amplitude of the correction turned out to be a few times V. The visibility functions $V(u, v, f)$ and $I(u, v, f)$ were then Fourier-transformed to obtain maps of the Stokes parameters on the sky at each frequency. Finally, we extracted from these maps the velocity profiles in I and V for each position on the sky.

In Figures 1*a* and 1*b* we present velocity profiles for I and V averaged over the entire source. These profiles are comparable to those obtained with a single-dish observation. We also

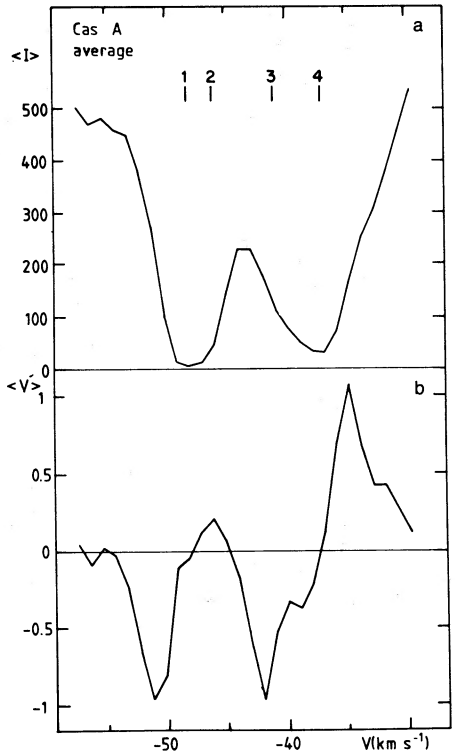

FIG. 1.—Velocity profiles of Stokes parameters (*a*) I and (*b*) V averaged over the face of Cas A. Tick marks denote the center velocities of the OH absorption line components for which the Zeeman effect has been detected by Heiles and Stevens (1985).

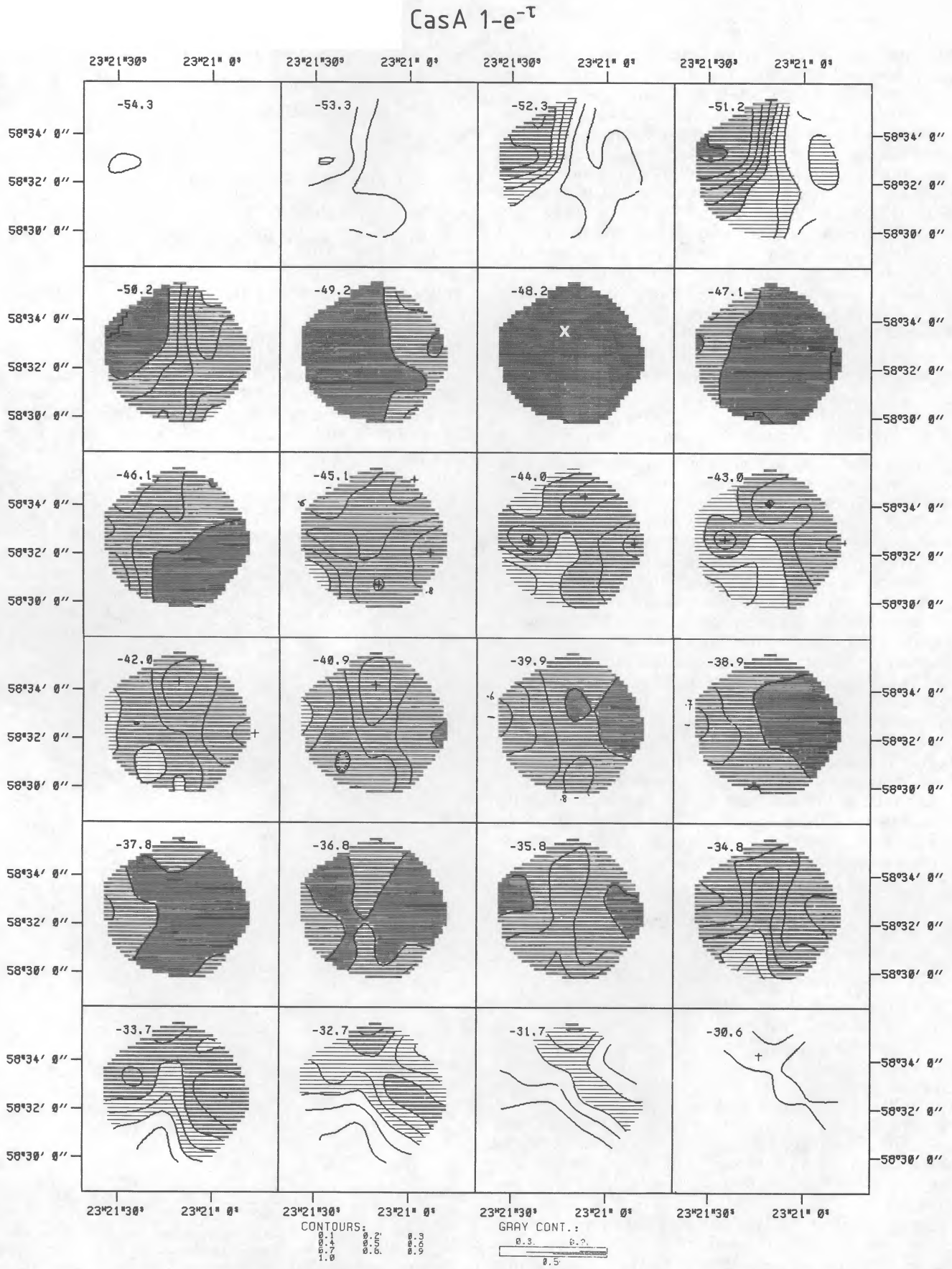

FIG. 2.—Maps of H I fractional absorption ($1 - e^{-\tau}$) toward Cas A for 24 Perseus arm velocity intervals between -54.3 and -30.6 km s^{-1}. Spatial resolution for these maps (and for those of Figs. 3 and 4) is 60″. Darker shadings are for higher fractional absorptions. Lightest shading represents fractional absorptions greater then 0.3; successively darker shadings represent fractional absorptions greater than 0.5 and 0.9, respectively. Contour lines are for absorptions of 0.1–1.0 in steps of 0.1.

derived values for the H I optical depth from the I maps and the continuum map of Cas A. These results are presented in Figure 2 and the form of maps for 24 velocity channels of the fractional absorption $(1 - e^{-\tau})$. Although the original maps have a resolution of $24'' \times 31''$, the maps of Figure 2 (and Figs. 3 and 4 described below) have been smoothed to a resolution of $60''$.

b) Problems in Computation of the Magnetic Field

The procedure of deriving the magnetic field from a least-squares fit to I and V over a selected range of channels (Paper I) requires that the field be constant over those channels. Using this procedure, we made many trials with the present data. It became clear that the values of B obtained, and their errors, are quite sensitive to the choice of channels in the fit. Therefore, we developed a different and more meaningful procedure which is outlined below.

The motivation for this method can be understood by making references to Figure 1. In the source-averaged I profile (Fig. 1*a*) there are two reasonably well-separated absorption features, whereas in the equivalent V spectrum (Fig. 1*b*) there are two negative-going dips and only one positive peak. This circumstance is not consistent with the simple picture of two separate absorbing clouds, each with its own characteristic velocity and uniform magnetic field; such a straightforward interpretation leads us to expect in the V spectrum a negative peak and a positive peak contributed by *each* cloud. The absence of a second positive peak in the V spectrum is not only evident in Figure 1*b*, but also in the V spectra at each sampled position across the face of Cas A (see, for an example, Fig. 5b [*solid line*]).

Do the high- and low-velocity Perseus arm absorption features originate in two discrete and physically homogeneous clouds of gas? This is certainly not the case, as can be seen immediately in Figure 2 where the complex structure of absorption varies rapidly with position and velocity. The H I absorption along the line of sight to Cas A must certainly arise from a superposition on the plane of the sky of gas concentrations having different velocities and, in many cases, high optical depths.

This circumstance can seriously alter the observed Zeeman profile, as the following hypothetical example illustrates. Consider two homogeneous H I clouds "A" and "B" along the line of sight to Cas A. Cloud A has a high optical depth but no magnetic field, and it lies directly in front of cloud B. The velocity of A is offset so that its peak optical depth is centered at a velocity for which the optical depth of B is at half maximum. Cloud B has a uniform magnetic field which contributes a standard s-shaped Zeeman pattern to the V profile. However, one peak of this s pattern is centered at the velocity for which the optical depth of foreground cloud A is a maximum. Therefore, this peak is absorbed, and the observed V profile contains just a single positive-going or a single negative-going peak rather than one of each.

The conclusion from this example is that we cannot always expect to find the typical Zeeman s pattern in the V spectrum if the absorption is strong and shows effects of blending or if the field is not uniform. Even the simple expectation that the integral of V across the profile is zero does not necessarily hold true.

c) Computation of the Field: A New Approach

In light of these complexities, we have developed a new method for computing magnetic fields from the Zeeman effect data. We no longer rely upon a least squares fit over a range of channels in the V and I profiles for a given position. Instead, we compute separate values for the line-of-sight magnetic field strength for each position across the face of the source and for each velocity channel. The resulting three-dimensional array of field values $B(\alpha, \delta, v)$ can then be assembled into a number of magnetic field maps (one for each velocity channel) that are analogous to the optical depth maps of Figure 2.

The procedure for computing $B(\alpha, \delta, v)$ is given below, where the explicit dependence upon (α, δ, v) has been omitted for the sake of brevity.

$$B = 2aV/(dI/dv)\ \mu\text{G} = 2V/g\ ; \tag{4}$$

where $g = (dI/dv)/a$, $a = 1690\ \mu\text{G/km s}^{-1}$ (for the H I line), V is the Stokes parameter V, $dI/dv = (I_{k+1} - I_{k-1})/2v_{ch}$, and $v_{ch} = 1.0$ km s^{-1}.

In Figure 3 we present maps of B computed in this fashion for the same 24 velocity channels of Figure 2. As for Figure 2, the map values are represented both by contour lines and by shading. Only values of B that meet the statistical criteria discussed in § III*e* below are shown.

d) The Statistical Error in B

The rms error $u(B)$ is dominated by the rms fluctuations $u(V)$ in V, which can be measured at positions off the continuum source. The error in g can be neglected. It follows that the absolute error in B is given by

$$u(B) = 2u(V)/g\ . \tag{5}$$

The relative error in B is given by

$$u(B)/B = (2/g) \times (g/2V) \times u(V) = u(V)/V\ . \tag{6}$$

We apply this result in the next section.

e) Cutoffs and Display of the Data

The derivation of B involves the division by g, making a cutoff g_c necessary. As a result, the error in B is not uniform across the source. In order to avoid the display of magnetic fields with large errors, we have applied a cutoff in such a way that fields with relative errors greater than 0.4 are not displayed in Figure 3. That is, we suppress B whenever V is less than or equal to V_c, where $V_c = 2.5u(V)$. However, Figure 3 has a serious ambiguity in that we cannot distinguish positions having no (or a very weak) field from those at which there is simply no information (i.e., $g < g_c$). Therefore, in Figure 4 we present another series of magnetic field maps in which the field strength is again represented by contour lines, but the shading now indicates the *error* (in μG) in the field measurement (lighter shadings refer to smaller errors). Comparison of figures 3 and 4 allows a resolution of the ambiguity described above. Note that we have also applied a cutoff in I at $\sim 7\%$ of the peak unabsorbed intensity, on the grounds that if the line is very staurated, no information exists about the magnetic field. Despite these cautions, the magnetic field maps of Figures 3 and 4 must still be interpreted with caution. Like ordinary synthesis maps of line optical depth, they are subject to the confusing effects of blending, and a single map limited to a very narrow range in velocity can provide misleading impressions. In § IV*b* below we discuss reasons for finding greater physical

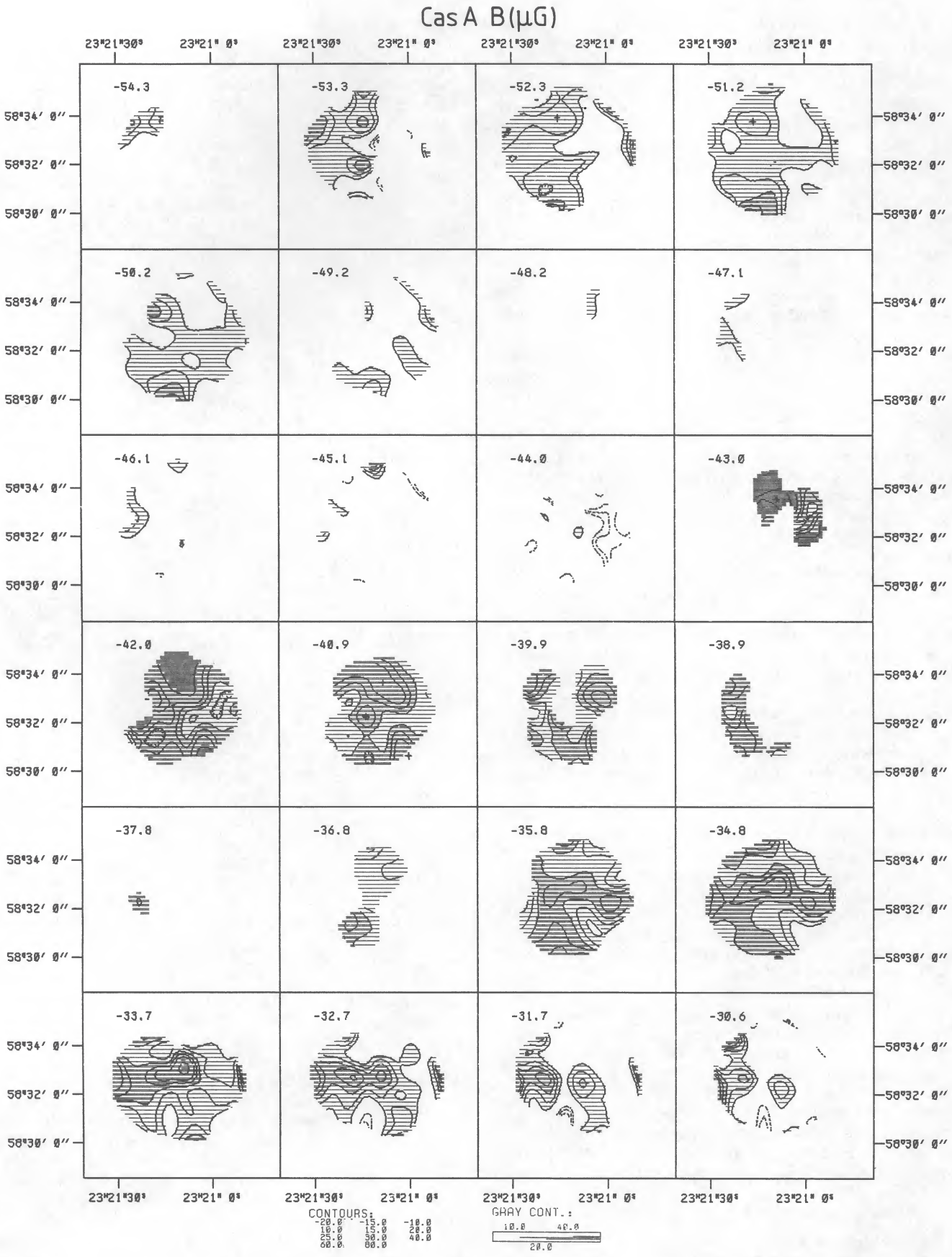

FIG. 3.—Maps of the line-of-sight component of the magnetic field toward Cas A for the same velocity intervals as Fig. 2. Darker shadings are for higher (i.e., more positive) fields, with the lightest shading for fields greater than 10 μG and successively darker shadings for fields greater than 20 and 40 μG, respectively. Contour lines are drawn for -20, -15, -10 μG (*dotted lines*) and for 10, 15, 20, 25, 20, and 40 μG (*solid lines*). Contour lines for $B = 5$ μG are not shown, since fields this msall cannot be reliably detected.

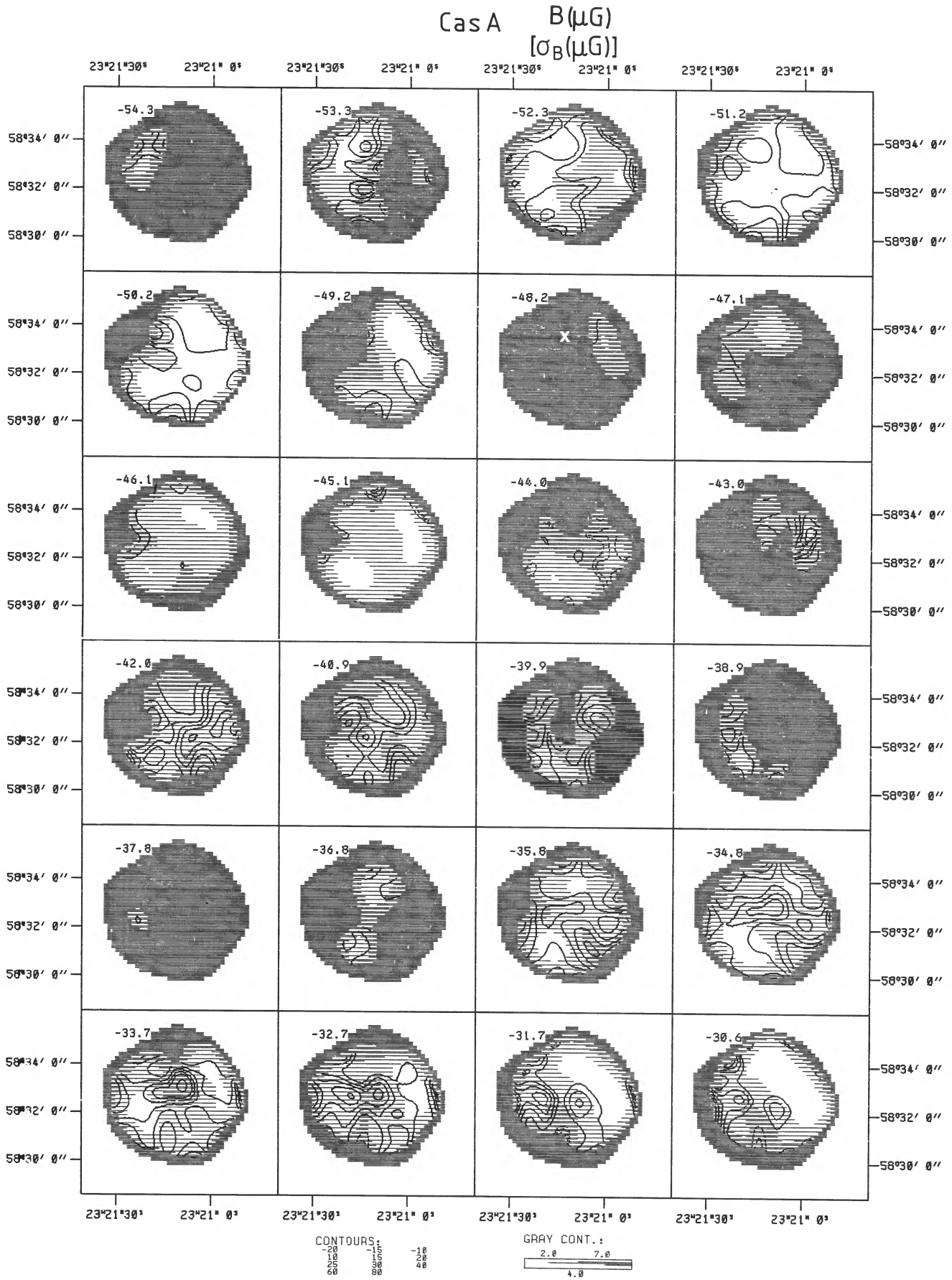

FIG. 4.—Maps of the line-of-sight component of the magnetic field toward Cas A. Contour lines in these maps are identical to those of Fig. 3. Shading, however, represents the rms error in the field strength, with darker shading for larger errors. Lightest shading represents an error greater than 2 μG. Successively darker shadings are for errors greater than 4 and 7 μG respectively.

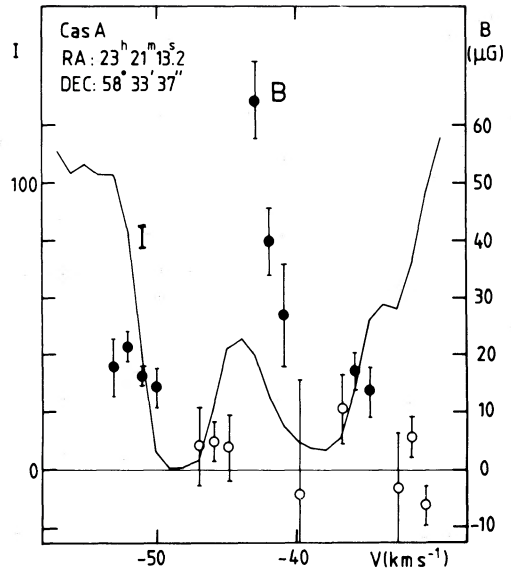

FIG. 5*a*

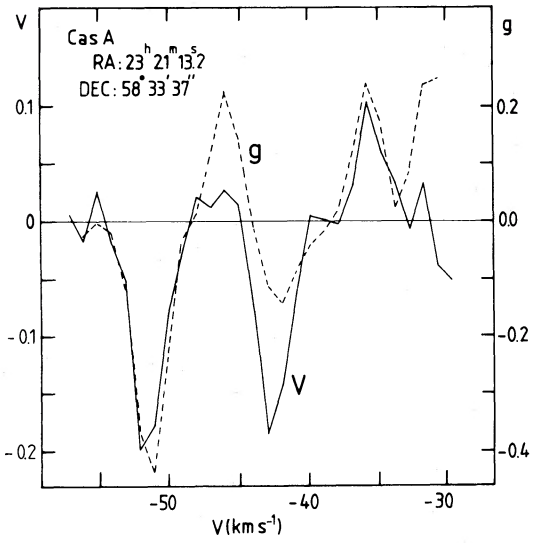

FIG. 5*b*

FIG. 5.—(*a*) Velocity profile of Stokes parameter *I* (*Solid line*) and of the line-of-sight component of the magnetic field (*circles*) for the position indicated by the "X" on the -48.2 km s^{-1} frame of Figs. 2 and 4. Filled circles are for field values that meet statistical tests for significance (see § IIIe), while open circles are for field values that do not meet tests. Vertical bar through each circle represents twice the standard deviation of the field value. (*b*) Profile of Stokes parameter *V* (*solid line*) and of the parameter "*g*" (*dashed line*, see eq. [4]) for the same position as Fig. 5*a*.

significance in the magnetic field maps at some velocities than at others.

In Figures 5 and 6 we present some alternate displays of the magnetic field data in order to illustrate the interplay of field strengths, errors, and cutoffs. Figure 5*a* shows (for the position shown by the "X" on the -48.2 km s^{-1} frames of Figs. 2 and 4) the *I* profile (*solid line*) and the *B* profile (*circles*), while Figure 5*b* shows the *V* profile (*solid line*) and the *g* profile (*dashed line*) for the same position. Recall that *g* is proportional to the derivatives of the *I* profile (eq. [4]). The mean errors of *B* are also shown in Figure 5*a*, where the total length of the error bar for each data point is $2u(B)$; that is, twice the standard deviation. The filled circles in this figure indicates that the relative error is above the cutoff [i.e., $V > 2.5u(V)$], while the open circles indicate the opposite. Values of the field that fall in this latter category are not shown in either Figure 3 or Figure 4.

In Figure 6 we present magnetic field values as a function of right ascension across the source for a given declination and velocity. Three cases are given for illustrative purposes: Figure 6*a* shows a weak but significant field (*V* is low and *g* is high); Figure 6*b* shows a weak but insignificant field (*V* is low, *g* is low), and Figure 6*c* presents a case of high field with large absolute but small relative errors (*V* is high and *g* is low). In Figures 6*a*–6*c* the meaning of the filled and open circles is the same as for Figure 5*a*.

IV. DISCUSSION

a) Magnetic Field Strengths toward Cas A

Figures 3 and 4 confirm the results of Paper I in showing that the magnetic field in the Perseus ar H I absorbing regions has small-scale structure, but it remains positive across the face of the source. (Positive field strengths represent lines of force directed *away from* the Sun.) In the high-velocity absorption component, the line-of-sight field strength is generally between 10 and 15 μG, with peaks as high as 25 μG. In the low-velocity component, field strengths are more variable and generally higher, ranging from less than 10 μG up to more than 40 μG. Note that a few negative field values do appear in maps for velocities between -32.7 and -30.6 km s^{-1}. However, references to Figure 4 reveals that these field values have large associated errors, and they are, at most, marginally significant.

b) Magnetic Field Strengths and Gas Distribution

We now reconsider the issue raised in Paper I of the morphological relationship between the field and H I optical

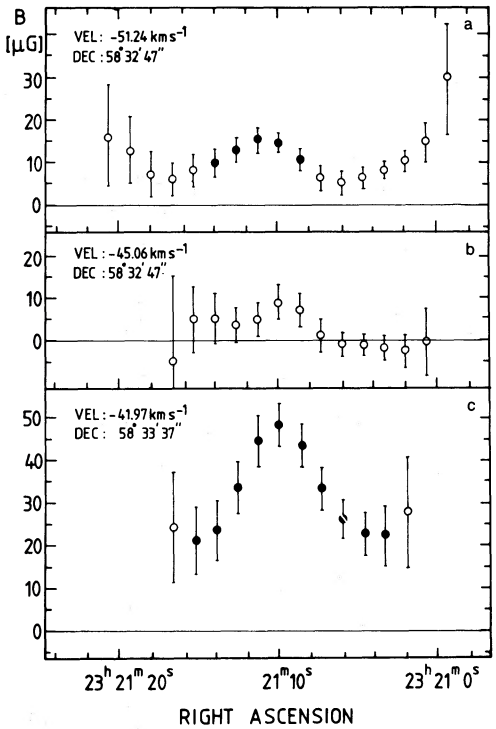

FIG. 6.—Three profiles of the line-of-sight magnetic field strength as a function of right ascension for fixed velocities and declinations. Profiles are chosen to illustrate various combinations of field strengths and errors (see § IIIe).

depths across the face of Cas A. If the field strength increases with increasing gas density, then a correlation is possible between the distributions of line-of-sight field values and H I optical depths across the source. Of course, an observed correlation of this sort need not exist even if field strengths and gas densities are related. For example, high H I optical depths along a particular line of sight can arise from locally lower excitation temperatures rather than from locally higher gas densities. Moreover, fluctuations in measured field strengths can arise from variations in the *direction* of the field just as well as from variations in true field strength. Nonetheless, if the field runs generally parallel to the line of sight toward Cas A, then variations in the line-of-sight field strength are less likely to arise from variations in geometry alone and more likely to represent real variations in the field strength.

These arguments notwithstanding, a comparison of Figure 2 and 3 reveals no obvious correlation between field strengths and H I fractional absorption. Consider, for example, the maps of B and H I absorption for velocities -52.3, -51.2, and -50.2 km s^{-1}. These velocities lie along the steep "outer" (i.e., most negative velocity) wing of the high-velocity absorption component. These velocities, therefore, are ones for which sensitivity to the Zeeman effect is high (i.e., g is high, see eq. [4]), yet the H I absorption is unsaturated. The B maps reveal a generally uniform field strength of typically 10 μG, with peaks of as much as 20–25 μG at the southern edge of the source. The H I maps, however, reveal a sharp east-west gradient with no particular features to the south.

Now consider the B and H I absorption maps for velocities -34.8, -33.7, and -32.7 km s^{-1}. These velocities lie along the steep "outer" (i.e., positive-velocity) wing of the low-velocity Perseus arm absorption component. The magnetic field maps show considerable spatial structure, with enhanced fields (of as much as 40 μG) lying primarily along an east-west magnetic "ridge" that passes through the center of the source. No such structure can be found in the equivalent maps of H I absorption, where, if anything, a ridge of enhanced values runs across the source in a north-south direction.

We must conclude that the B maps and the H I maps are not alike. Either the magnetic field is not enhanced in regions of higher H I gas density, or fluctuations in field direction rather than strength are largely responsible for spatial structure in the B maps, or the run of H I optical depths across the face of the source is not real indicator of variations in H I volume density.

We believe that this last possibility is the most probable. The densest H I gas along the line of sight to Cas A may be concentrated in relatively small regions. However, absorption measurements are sensitive to *column* densities, not volume densities, and regions of large volume density do not necessarily stand out in the absorption profiles. This circumstance suggests that a potentially more fruitful comparison might be made between the magnetic field maps of Figures 3 and 4 and the distribution of *molecular* gas. For this purpose, the molecular gas serves only as a tracer of associated (and presumably enhanced-density) H I, since the magnetic fields we derive are not relevant to the molecular regions themselves.

GKD, in their aperture synthesis study of Perseus arm H_2CO absorption toward Cas A, identify a number of small clumps of molecular gas. These clumps have angular sizes of between $\sim 10''$ and $30''$. Comparing the molecular clumps with the H I synthesis maps of Kalberla, Schwarz and Goss (1985*a*); GKD identify small angular scale enhancements in H I absorption that coincide in position with most of the clumps. These enhancements are typically 2–3 times larger in diameter than the associated molecular clumps, and they account for only a small fraction of the total H I optical depth, typically no more than $\sim 20\%$. GKD suggest on theoretical grounds that the H I enhancements are shells surrounding the molecular clumps and protecting them from the interstellar radiation field. Other geometries are possible, however (see Heiles and Stevens 1985). In the discussion that follows we refer to these H I enhancements associated with the molecular clumps as "H I clumps."

The H_2CO maps of GKD for -48.6 and -46.2 km s^{-1} reveal a preponderance of molecular clumps near the south and southeast edges of the source. Bieging and Crutcher (1985) find a similar distribution of OH in their VLA maps, and Troland, Crutcher, and Heiles (1985) find enhanced CO emission at the southern edge of Cas A which is obviously related to a peak in CO emission located ~ 8 southeast of the source center. The peak in magnetic field strength, visible in maps made for velocities -52.3 – -50.2 km s^{-1} (Fig. 3), corresponds quite closely in position to the clumps of molecular gas.

In making this comparison between magnetic field and molecular gas distributions, we have chosen maps of each made at different velocities. That is, we compare the H I Zeeman effect measured at velocities of about -52 to -50 km s^{-1}, with H_2CO optical depths at velocities of about -49 to -46 km s^{-1}. However, this choice of different velocities is inevitable, since the molecular lines are much narrower than the H I absorption lines and since the Zeeman effect is detected most sensitively at velocities corresponding to the steep wings of the H I lines. Moreover, the H I clumps, wherein we measure the field, need not have the same velocity widths or even exactly the same center velocities as the molecular clumps associated with them.

We now compare the magnetic field maps between -24.8 and -32.7 km s^{-1} with the H_2CO data of GKD. These authors present a map of integrated H_2CO optical depth for the velocity range -45 to -30 km s^{-1}, in which molecular clumps are concentrated along an east-west ridge passing through the center of the source. The OH maps of Bieging and Crutcher and the CO maps of Troland, Crutcher, and Heiles (1985) show similar distributions. Such morphology in the molecular gas distribution is quite similar to the magnetic ridge described above.

As a further illustration of the relationship between the magnetic field structure and the H I clumps, we present in Figure 7 a schematic illustration of these clumps. Each is represented by a circle having the angular size given by GKD; that is, the geometric mean of major and minor axes after correcting for instrumental beam effects. The Roman numeral labels are taken from GKD, and the dashed outline of Cas A denotes the source boundary within which H I absorption is shown in Figure 2. H I masses estimated for these clumps by GKD range over about one order of magnitude (0.2–1.8 $M_\odot$), while the estimated H_2 masses for the corresponding molecular clumps vary by more than two orders of magnitude (0.2–66 $M_\odot$). (Note, however, that the H_2 masses may be much smaller, as discussed in § IV*d*, below.) As a visual guide to the difference in mass, we have used shading in Figure 7 to denote H I clumps having unusually large masses (vertical lines if $M_{\rm H\,I} > 1.5\ M_\odot$) and molecular clumps having unusually large masses (horizontal lines if $MH_2 > 10\ M_\odot$).

The schematic illustration of Figure 7 reinforces the idea that the H I clumps are related to structure in the magnetic field. Only clump V is associated with the high-velocity H I

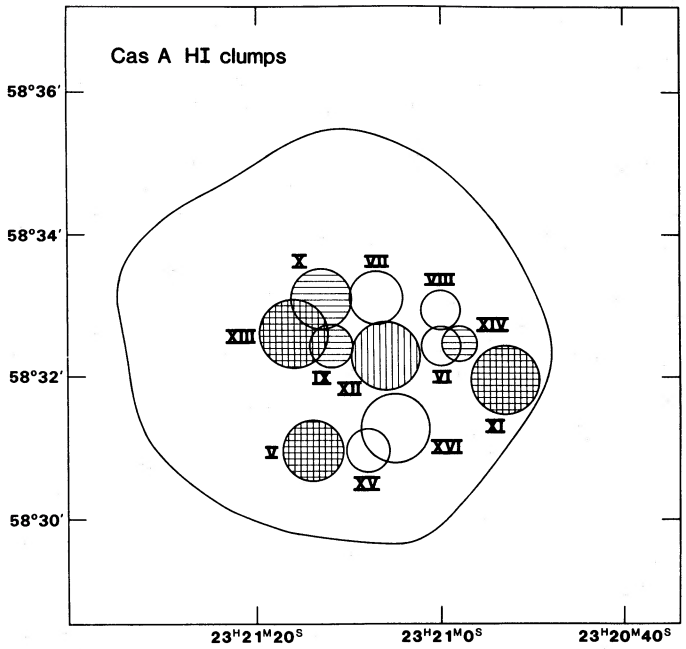

FIG. 7.—Schematic diagram of the H I enhancements found by Goss *et al.* (1985) to be associated with clumps of molecular gas. These features are referred to in text as "H I clumps." Each circle is labeled with a Roman numeral taken from Goss *et al.*. Size of each circle represents the geometric mean of major and minor axes of the half-intensity contour. Circles with vertical shading have relatively high H I masses, while circles with horizontal shading have relatively high molecular masses, as estimated by Goss *et al.* (see § IV*b*.) Dashed outline represents same field of view for Cas A as that shown in maps of Fig. 2.

component. (Other H I clumps presumably exist at these higher velocities; however, large H I optical depths from unrelated gas render such shells too difficult to detect.) H I clump V has a large mass, as does its associated molecular clump. The two are positioned only very slightly north (30″) of the magnetic field peak visible in Fig. 3 at velocities near -51 km s^{-1}. Of the remaining H I clumps, all are associated with the low-velocity H I component, and only five have appreciable H I (or corresponding H_2) masses (IX, X, XI, XIII, and XIV). Each is well positioned along the magnetic ridge in Figure 3 visible at velocities near -33 km s^{-1} Clump XI is notable in that it has the largest H I and the largest H_2 mass of all, and Figure 3 exhibits a corresponding peak in magnetic field strength at velocities near -33 km s^{-1}.

In summary, peaks in magnetic field at -51 and -33 km s^{-1} often coincide with molecular clumps at adjacent velocities. This spatial correspondence suggests that we have obtained the first observational evidence for the theoretically expected increase in magnetic field strength with interstellar gas density.

The magnetic fields measured toward Cas A do not of course, arise solely within the H I clumps. The measured fields also reflect magnetic conditions in the more diffuse H I gas about them. Since the clumps account only for only a small fraction of the H I optical depth, relatively small enhancements of the *observed* field in the direction of a clump (typically a factor of 2; see Fig. 3) may imply much larger enhancements of the field within the clump itself. However, this need not be true if the velocity dispersion of the clump is small relative to that of the overall H I absorption component. Indeed, the velocity dispersions of the H I clumps *are* small, typically 2–3 km s^{-1} (GKD). In this case, we find from simple numerical experiments that a twofold increase in observed field strength toward a clump can arise from a threefold increase in actual field strength within the clump. Since the observed fields in the direction of the H I clumps are in the range 20–40 μG, the actual fields within the clumps may be of order 3/2 times greater, or 30–60 μG. While relatively high, these values are comparable to magnetic field strengths measured in the H I absorbing region in front of Orion A (see § IV*d*, below).

Note that we have not considered in the foregoing discussion the magnetic field maps for velocities corresponding to the "inner" edges of the Perseus arm absorption components (for example, -46.1, -45.1, -42.0, and -40.9 km s^{-1}). Some of these maps do exhibit pronounced spatial structure, although this structure does not resemble the distribution of H I or molecular clumps. The maps at -42.0 and -40.9 km s^{-1} even have magnetic peaks in the northern sector of the source that coincide with peaks in H I optical depth in Figure 2. However, the physical significance of field structure at these intermediate velocities is open to question. The inner edges of the two H I absorption features are far more likely to be affected by confusion arising from blending of different velocity components than are the outer wings of the same two features. Also, the errors in the *B* maps at the inner velocities are generally greater than the errors in the maps at the outer velocities. For these reasons, we believe that the most physically meaningful maps of Figures 3 and 4 are those at velocities corresponding to the two outer edges of the Perseus arm H I absorption features; that is, velocities within ~ 1 or 2 km s^{-1} of -51 and -33 km s^{-1}.

c) Virial Energies and Energy Densities

We now consider the virial equilibrium of these clouds. As GKD and as Heiles and Stevens (1985) point out, the molecular clumps are not gravitationally bound. This conclusion is especially warranted if one includes in the virial equation a term representing the macroscopic motions that must exist within the clumps. (The observed H_2CO velocity dispersions are considerably wider than thermal dispersions alone.) Nor are the molecular clumps maintained in equilibrium by external gas pressure, since the virial terms for surface pressure are negligible. Similar conclusions about virial stability apply to the H I clumps as well. Both atomic and molecular clumps are evidently in a transient state of dynamic evolution, and they should be expanding in some way. This circumstance could arise if the atomic and molecular gas has been recently affected by a shock wave, as discussed by Heiles and Stevens (1985).

To assess the effects that are most important in controlling the evolution of the clumps, we have used the simple expedient of computing energy densities arising from thermal motions, from macroscopic motions, and from magnetism. For representative values of gas density (350 cm^{-3}) and velocity width (2.5 km s^{-1}) in the H I clumps (GKD) and for a kinetic temperature of 50 K and a magnetic field of 50 μG, we find that the energy densities associated with the magnetic field are 5 times larger than those associated with macroscopic motions. Thermal energy densities are negligible. Evidently, the magnetic field has a dominant influence upon dynamics of the gas in the atomic clumps. A corollary to this statement is that the field is not significantly tangled within them. The situation for the molecular clumps is less clear because both the H_2 volume

density and the total magnetic field strength are uncertain (see Heiles and Stevens 1985 for a full discussion).

d) Why Are Cas A Field Strengths So High?

The maps of Figure 3 indicate that magnetic fields along the line of sight to Cas A reach values of 40 μG or more. Magnetic fields measured in other H I regions via the Zeeman effect are almost always much smaller, typically ~ 10 μG or less (e.g., Heiles and Troland 1982; Troland and Heiles 1982*b*; Heiles 1985). Another high field region is Orion A, where the field in the H I absorption region is ~ 50 μG when measured with a single dish (Verschuur 1969*b*; Brooks, Murray, and Radhakrishnan 1971), and in places it exceeds 70 μG in the H I Zeeman synthesis map of Troland, Heiles, and Goss 1985).

The Orion absorption region most probably lies at the periphery of the H II region, perhaps in the nebular boundary zone that separates the ionized gas from the surrounding neutral cloud (Lockhart and Goss 1978). Higher-than-normal gas densities and field values may have arisen in such a region as a result of shocks driven by the expanding ionized gas or else during the contraction phase of the progenitor interstellar cloud.

No H II regions are known to lie directly along the line of sight to Cas A. However, the longitude range 108°–116° is relatively rich in emission nebulae at Perseus arm distances (Fich and Blitz 1984), and the supernova remnant itself appears to be embedded in a complex of H II regions spread out over a few degrees in the sky (Fich 1985). Furthermore, Cas A lies in the general direction of an unusually large (100 pc long) Perseus arm molecular complex centered at about $l = 111°$ and visible in the CO maps of Cohen *et al.* (1980). Parts of this complex also appear in the ^{13}CO maps of Casoli, Combes, and Gerin 1984). Evidently, the line of sight to Cas A is associated with regions of star formation in the galaxy. It is quite likely that the processes creating these regions, or arising as a result of star formation within them, are at least partly responsible for the unusually high magnetic fields in the direction of Cas A, as well as of Orion A.

A related question about the magnetic field in the Cas A H I clouds is this: why are the field strengths in the low-velocity feature ~ 2 times greater than those in the high-velocity feature? A clue to the origin of this difference may lie in the ^{13}CO maps of Casoli, Combes, and Gerin (1984). These maps show the distribution of molecular gas in 23 contiguous Perseus arm velocity intervals for a field $1^\circ.3 \times 1^\circ.3$ immediately south of Cas A. Very little molecular gas appears at velocities corresponding to the *high*-velocity H I features. However, in the maps corresponding to the low-velocity H I features, a large gas complex is clearly apparent. This complex does not actually overlap the Cas A position in the maps, although CO does indeed exist at these velocities in the direction of the source (Troland, Crutcher, and Heiles 1985). Nonetheless, unless the CO-bearing gas lies behind Cas A, then the line of sight to the source passes close to an extended molecular region having a velocity of between -43 and -33 km s^{-1}. This velocity range corresponds very closely to that of the low-velocity H I gas, and the higher magnetic fields encountered at these velocities may reflect a specific association between the H I and the denser molecular gas.

Nature has shown a rare kindness to Zeeman effect observers by providing such a strong continuum source in so fortuitous a direction in the Galaxy. What is more, nature has offered us the additional consideration of scheduling the supernova itself (circa 1660: Kamper and van den Bergh 1976) such that the resulting remnant is still radio-bright now, when we have the technical ability to utilize it for Zeeman-effect studies.

V. SUMMARY

Through the application of aperture synthesis techniques to the Cas A H I Zeeman effect, we have created the first velocity-resolved maps of interstellar magnetic fields (Figs. 3 and 4). The spatial resolution of these maps is 1′ or ~ 1 pc at a distance of 3 kpc. Along most lines of sight to Cas A, the parallel component of the field is in the range 10–20 μG. Localized peaks in the observed field strength reach values of 20–40 μG, with the highest values occurring in the low-velocity absorption component.

Peaks in magnetic field strength bear no obvious relation to maps of overall H I optical depth toward Cas A. However, the peaks do coincide closely with the positions of small-scale molecular clumps. These clumps, in turn, coincide with small enhancements in H I optical depth, identified by GKD as regions of higher density H I, and referred to here as H I clumps. We argue that the magnetic peaks in our maps result from enhancements in the local magnetic field in the H I clumps. Therefore, fields in the H I clumps must be between 30 and 60 μG or higher, and we have discovered the first observational evidence for the increase of magnetic field strength with interstellar gas density.

Neither the molecular clumps nor the H I clumps can be in virial equilibrium. They must be in a state of dynamical evolution, perhaps rebounding from the effects of a shock wave. On the basis of energy density considerations, we find that the magnetic field in the H I clumps has a dominant influence upon them; thus, the field lines should not be significantly tangled.

The generally high magnetic field strengths in H I regions toward Cas A probably result from the passage of the line of sight through regions of molecular clouds and active star formation.

The WSRT is operated by the Netherlands Foundation for Radio Astronomy, with financial support from the Netherlands Organization for the Advancement of Pure Research (Z.W.O.). The data reduction for this study was partly carried out using the computing facilities of the University of Groningen Computing Center. This work was supported in part by the US National Science Foundation to C. H.

REFERENCES

Batrla, W., Walmsley, C. M., and Wilson, T. L. 1984, *Astr. Ap.*, **136**, 127.
Beiging, J., and Crutcher, R. M. 1985, in preparation.
Bos, A., Raimond, E., and van Someren Greve, H. W. 1981, *Astr. Ap.*, **98**, 251.
Bregman, J. D., Troland, T. H., Forster, J. R., Schwarz, U. J., Goss, W. M., and Heiles, C. 1983, *Astr. Ap.*, **118**, 157.
Brooks, J. W., Murray, J. D., and Radhakrishnan, V. 1971, *Ap. Letters*, **8**, 121.
Casoli, F., Combes, F., and Gerin, M. 1984, *Astr. Ap.*, **133**, 99.
Cohen, R. S., Cong, H., Dame, T. M., and Thaddeus, P. 1980, *Ap. J. (Letters)*, **239**, L53.
Fich, M. 1985, in preparation.
Fich, M., and Blitz, L. 1984, *Ap. J.*, **279**, 125.
Goss, W. M., Kalberla, P. M. W., and Dickel, H. R. 1985, *Astr. Ap.*, **139**, 317.
Greisen, E. W. 1973, *Ap. J.*, **184**, 363.
Heiles, C. 1985, in preparation.
Heiles, C., and Stevens, M. 1985, *Ap. J.*, **301**, 331.
Heiles, C., and Troland, T. H. 1982, *Ap. J. (Letters)*, **260**, L23.
Kalberla, P. M. W., Schwarz, U., and Goss, W. M. 1985, in preparation.
Kamper, K., and van den Bergh, S. 1976, *Ap. J. Suppl.*, **32**, 351.

Lockhart, I. A., and Goss, W. M. 1978, *Astr. Ap.*, **67**, 355.
Troland, T. H., Crutcher, R. M., and Heiles, C. 1985, *Ap. J.*, **298**, 808.
Troland, T. H., and Heiles, C. 1982*a*, *Ap. J.*, **252**, 179.
———. 1982*b*, *Ap. J.* (*Letters*), **260**, L19.
Troland, T. H., Heiles, C., and Goss, W. M. 1985, in preparation.
Verschuur, G. L. 1969*a*, *Ap. J.*, **156**, 861.
———. 1969*b*, *Nature*, **233**, 140.
Weiler, K. W., and Raimond, E. 1976, *Astr. Ap.*, **52**, 397.

J. S. ALBINSON and J. D. BREGMAN: Netherlands Foundation for Radio Astronomy, Postbus 2, NL-7990 AA Dwingeloo, the Netherlands

W. M. GOSS and U. J. SCHWARZ: Kapteyn Astronomical Institute, Postbus 800, NL-9700 AV Groningen, the Netherlands

CARL HEILES: Astronomy Department, University of California, Berkeley, Berkeley, CA 94729

T. H. TROLAND: Physics and Astronomy Department, University of Kentucky, Lexington, KY 40506